Chiral flexural waves in structured plates: directional localisation and control

G. Carta[a,*], D. J. Colquitt[b], A. B. Movchan[b], N. V. Movchan[b], I. S. Jones[a]

[a] *Liverpool John Moores University, Mechanical Engineering and Materials Research Centre, Liverpool, L3 3AF, UK*
[b] *University of Liverpool, Department of Mathematical Sciences, Liverpool, L69 7ZL, UK*

Abstract

A new class of elastic waveforms, referred to as "chiral flexural waves", is introduced for a multi-structure, which encompasses an elastic plate connected to a system of elastic flexural rods with gyroscopic spinners. The junction conditions describing the connection between the plate and the thin flexural rod require logarithmic asymptotics. The directional preference of the system is governed by the motion of gyroscopic spinners. For doubly-periodic chiral multi-structures studied here, parabolic modes associated with strong dynamic anisotropy of Bloch-Floquet waves are identified. Closed form analytical findings are accompanied by numerical simulations, which identify one-way flexural waves propagating along a straight interface in a flexural chiral system, without requiring the presence of Dirac cones on the dispersion surfaces.

Keywords: Flexural waves, Structured plate, Active chirality, Dispersion, Parabolic metamaterial, One-way unidirectional wave propagation

1. Introduction

Chirality, the property of an object such that it cannot be superimposed onto its mirror image [1], is used in many fields of science. In elasticity, chirality has been exploited both in statics, particularly in design of auxetic media [2–5], and in dynamics, with the aim of modifying the dispersive properties of honeycomb discrete structures [6–8]. It has also been used to attain low-frequency broadband vibration suppression in flexural systems [9, 10]. A continuous chiral metamaterial connected to inertial resonators by means of inclined ligaments was proposed in [11] for filtering and focussing purposes. A chiral lattice with tilted resonators was studied in [12, 13] to couple pressure and shear waves

*Corresponding author
Email addresses: giorgio.carta@liverpool.ac.uk (G. Carta), d.j.colquitt@liverpool.ac.uk (D. J. Colquitt), abm@liverpool.ac.uk (A. B. Movchan), nvm@liverpool.ac.uk (N. V. Movchan), i.s.jones@ljmu.ac.uk (I. S. Jones)

and to create localised interfacial waveforms. Homogenisation techniques for periodic chiral cellular solids were discussed in [14].

In this paper, we study a flexural system possessing "active chirality", produced by the mechanical action of gyroscopic spinners. The system considered is a plate with "chiral resonators", consisting of beams connected to gyroscopic spinners. The analytical linearised formulation for the connection between an Euler-Bernoulli beam and a gyroscopic spinner was developed in [15, 16], where gyroscopic boundary conditions were derived and a physical interpretation of a *gyrobeam* (used in [17–21]) was provided. Discrete systems attached to gyroscopic spinners were investigated in [22–24].

In the chiral flexural system examined in this paper, two phenomena can be observed at specific frequencies: parabolic modes and one-way unidirectional wave propagation. Parabolic modes are associated with waves propagating along a single line. In the present paper, it will be shown that parabolic modes can be generated in the system with either chiral resonators (beams with gyroscopic spinners) or non-chiral resonators (beams with masses having translational and rotational inertia); however, the structure with chiral resonators shows stronger directional preference. Although parabolic modes have already been detected in elastic systems, such as elastic lattices [24, 25], to the best of our knowledge this is the first time that they are observed in a chiral structured plate.

The present flexural system with chiral resonators is also capable of supporting one-way unidirectional interfacial waves, as shown in Fig. 1. This phenomenon can be obtained by dividing the domain into two regions with gyroscopic spinners rotating in opposite directions, and applying a force close to the interface between the two regions. Unidirectional propagating edge modes immune to backscattering were initially detected in photonic crystals (see, for example, [26–30]). These modes are analogous to the edge states associated with the quantum Hall effect [26]. In elasticity, the possibility of creating unidirectional edge modes has been demonstrated in platonic crystals [31–35], mechanical granular graphene [36], systems incorporating coupled pendula [37] and lattices with gyroscopic spinners [38–40]. Here, it will be shown that the main difference between the present paper and previous works on topological protection is that non-trivial topological stop-bands, associated with breakage of Dirac cones, are not needed to generate one-way unidirectional propagating modes in the structure.

Transmission and reflection of flexural waves in elastic plates with periodic stacks of obstacles have been extensively studied in [41–46]. In particular, transmission resonances and trapped modes were observed in several frequency regimes for the appropriate angles of incidence. Interaction of time-harmonic plane flexural waves with semi-infinite systems of spring-mass resonators was studied in [45]. The effects of negative inertia and associated localised modes for systems of spring-mass resonators were discussed in [47].

Compared to the previous work, we describe a new type of wave phenomena referred to as a "chiral flexural wave". In the standard scalar formulation for a fourth-order problem associated with the out-of-plane flexural displacement, chiral waves are not possible. However, chirality can be introduced by using

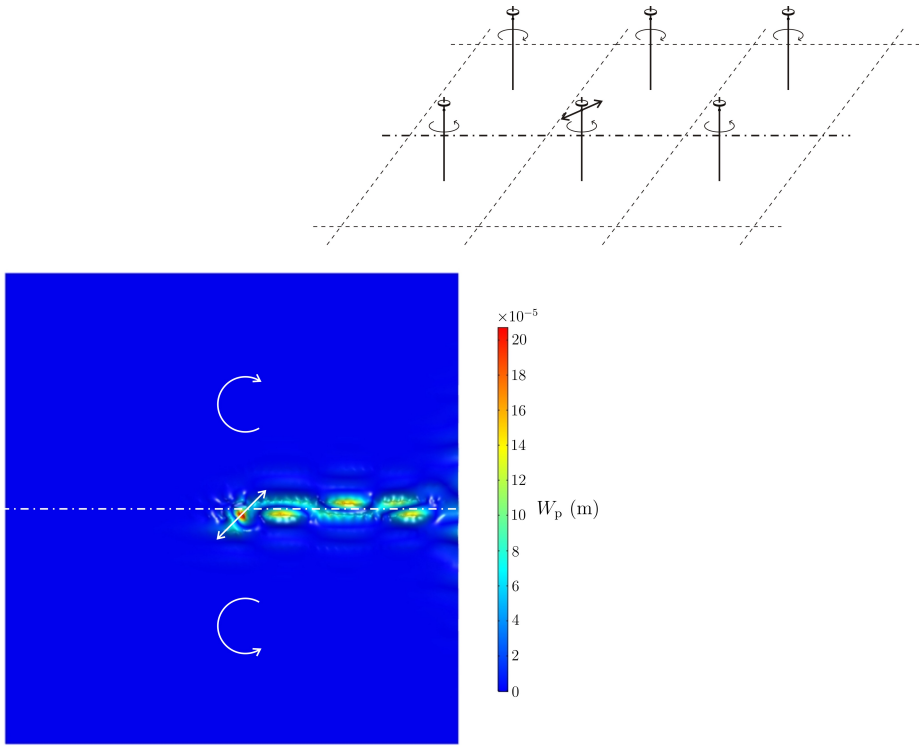

Figure 1: One-way unidirectional wave in a plate with a finite array of chiral resonators, consisting of beams attached to gyroscopic spinners. The structure is divided into two domains, characterised by opposite values of the gyricity Ω (see Section 2), and is excited by a time-harmonic force, represented by the arrow, applied to the tip of a beam in the lower domain. The transverse displacement amplitude in the plate W_{p} is plotted. The inset shows a detail of the system in proximity of the interface. The elementary cell is represented by a rectangular plate, with a beam attached at its centre and a gyroscopic spinner connected to the tip of the beam. The gyroscopic spinners above and below the interface rotate in opposite directions. The values of the parameters are given in Section 4.

a system of flexural resonators incorporating gyroscopic spinners. In order to account for the coupling of moments between the resonators and the plate, it is necessary to derive a new type of logarithmic junction condition. Such a coupling is neglected when the plate is connected to other types of resonators (for instance, masses and spring-mass oscillators analysed in [32, 45, 47]) as well as when the beam is represented by a one-dimensional segment with a cross-section of zero radius. Our novel asymptotic analysis takes the shape of the cross-section into account and enables us to compute asymptotic approximations of moments exerted on the elastic plate. This gives rise to novel dispersion properties of flexural waves in chiral structured plates.

We show that in the elementary cell of the doubly-periodic system, the transverse displacement $W_{\rm p}$ of the plate with flexural stiffness D satisfies the equation

$$D\Delta^2 W_{\rm p} - N_z(0)\delta(\boldsymbol{x}) + M_x(0)\frac{\partial}{\partial y}\delta(\boldsymbol{x}) - M_y(0)\frac{\partial}{\partial x}\delta(\boldsymbol{x}) = 0\,, \qquad (1)$$

where $\boldsymbol{x} = (x, y)$, Δ^2 is the biharmonic operator and $\delta(\boldsymbol{x})$ is the Dirac delta function. For simplicity, the mass density of the plate itself is assumed to be zero. The origin is placed at the junction region between the plate and the elastic beam. The coefficients $N_z(0)$, $M_x(0)$ and $M_y(0)$ represent the axial force and bending moments transmitted by the chiral resonators to the plate at the junction, where $z = 0$. When other types of resonators (such as masses or spring-mass oscillators) are connected to the plate, only $N_z(0)$ is different from zero. We also note that logarithmic asymptotic approximations are required for $M_x(0)$ and $M_y(0)$, and these are discussed in the main text of the paper.

The paper is organised as follows. In Section 2, we describe the chiral flexural system, represented by a beam attached to a plate at one end and connected to a gyroscopic spinner at the other end. The effect of the gyroscopic spinner is modelled by appropriate boundary conditions [16] on the beam. We develop the junction conditions between the beam and the plate using the novel concept of "logarithmic rotational spring". In addition, we solve analytically the eigenvalue problem for a circular plate which is clamped at the boundary and has a chiral resonator at the centre. We compare the analytical results with the outcomes obtained from finite element computations. In Section 3, we determine the dispersion diagrams for a periodic array of chiral resonators on a flexural foundation, both analytically and numerically. In particular, we identify frequencies at which parabolic modes may occur. In Section 4, we demonstrate the possibility of creating one-way unidirectional interfacial waves in the flexural system. In Section 5, we perform additional simulations to show how parabolic modes can be generated in the structure. Finally, in Section 6 we provide concluding remarks.

2. Eigenvalue problem for a chiral resonator on a flexural foundation

In this section, we consider a model problem for the evaluation of the eigenfrequencies of an elastic multi-structure, consisting of a circular thin plate in the

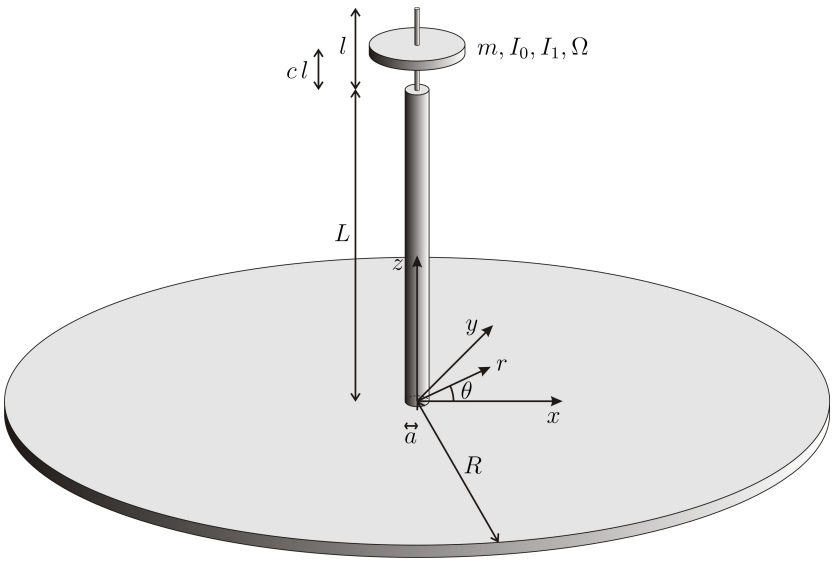

Figure 2: Elastic multi-structure, made of an elastic beam connected at one end to a gyroscopic spinner and at the other end to the centre of a circular plate, clamped on the boundary and with radius R. The beam has length L and circular cross-section of radius a. The length of the gyroscopic spinner is denoted by l, and $c\,l$ represents the distance of the centre of mass of the spinner relative to the base of the spinner.

xy-plane and a beam attached to the centre of the plate (see Fig. 2). The plate is clamped on the boundary and the beam axis is collinear with the z-axis. We assume that the tangent to the beam axis always remains orthogonal to the plate at the junction. The other end of the beam is connected to a gyroscopic spinner of given mass, moments of inertia and *gyricity* (introduced in [15, 16]).

The plate and beam are modelled using Kirchhoff and Euler-Bernoulli theory, respectively. These models are accurate in the low- and mid-frequency ranges. For higher frequencies, higher-order approximations (for example, Timoshenko theory for the beam and Mindlin theory for the plate) should be used to better describe the behaviour of the real system.

In general the gyroscopic motion is not periodic, but in the linearised case we can identify harmonics which constitute the representation of the fields over a given time interval [15, 16]. By linearisation we mean that the angle of nutation is small at any time during the motion of the gyroscopic system. Since the system of equations governing the motion of the gyroscopic spinner has been linearised (see [15, 16]), stability is not an issue and will not be considered in this paper.

The equation which governs the time-harmonic motion of the Kirchhoff plate outside the junction region with the elastic beam is

$$\Delta^2 W_{\rm p} - \beta_{\rm p}^4 W_{\rm p} = 0\,, \quad \text{with } \beta_{\rm p} = \left(\frac{\rho_{\rm p} h \omega^2}{D}\right)^{1/4}. \tag{2}$$

Here $W_\mathrm{p} = W_\mathrm{p}(r,\theta)$ is the displacement amplitude of the plate in the z-direction, Δ^2 is the biharmonic operator, β_p is the frequency-like parameter for the plate, ω is the radian frequency, h is the thickness of the plate, ρ_p is the density, and $D = E_\mathrm{p}h^3/[12(1-\nu_\mathrm{p}^2)]$ is the flexural stiffness of the plate, where E_p and ν_p are the plate's Young's modulus and Poisson's ratio, respectively. The radius of the circular plate is denoted by R.

For the vertical beam, the displacement amplitudes U_b, V_b and W_b in the x-, y- and z-direction, respectively, satisfy the equations

$$\begin{aligned} &U_\mathrm{b}'''' - \beta_b^4 U_\mathrm{b} = 0\,, \quad V_\mathrm{b}'''' - \beta_b^4 V_\mathrm{b} = 0\,, \quad \text{with } \beta_\mathrm{b} = \left(\frac{\rho_\mathrm{b} A_\mathrm{b}\omega^2}{E_\mathrm{b} J_\mathrm{b}}\right)^{1/4}, \\ &E_\mathrm{b} W_\mathrm{b}'' + \rho_\mathrm{b}\omega^2 W_\mathrm{b} = 0\,, \end{aligned} \tag{3}$$

where the derivatives are taken with respect to the longitudinal coordinate z. In (3) β_b is the frequency-like parameter for the beam, A_b and J_b are the area and second moment of area of the beam cross-section respectively, and E_b and ρ_b are the Young's modulus and density of the beam. In this section, we consider a beam with circular cross-section of radius a.

As shown in [15, 16], the effect of the gyroscopic spinner can be reproduced by a set of boundary conditions, representing the balances of linear and angular momenta:

$$\begin{aligned} &E_\mathrm{b} J_\mathrm{b} \boldsymbol{\mathcal{V}}_\mathrm{b}''(L) = \boldsymbol{\mathcal{A}}\boldsymbol{\mathcal{V}}_\mathrm{b}'(L)\,, \\ &E_\mathrm{b} J_\mathrm{b} \boldsymbol{\mathcal{V}}_\mathrm{b}'''(L) = -m\omega^2 \boldsymbol{\mathcal{V}}_\mathrm{b}(L) - m\omega^2 c\, l \boldsymbol{\mathcal{V}}_\mathrm{b}'(L)\,, \\ &E_\mathrm{b} A_\mathrm{b} W_\mathrm{b}'(L) = m\omega^2 W_\mathrm{b}(L)\,, \end{aligned} \tag{4}$$

where

$$\boldsymbol{\mathcal{V}}_\mathrm{b}(z) = \begin{pmatrix} U_\mathrm{b}(z) \\ V_\mathrm{b}(z) \end{pmatrix} \quad \text{and} \quad \boldsymbol{\mathcal{A}} = \begin{pmatrix} I_0\omega^2 & -\mathrm{i}\omega I_1\Omega \\ \mathrm{i}\omega I_1\Omega & I_0\omega^2 \end{pmatrix}. \tag{5}$$

Here m is the mass of the spinner, L and l are the lengths of the beam and the spinner respectively, c is the parameter which characterises the distance $c\,l$ of the spinner centre of mass with respect to the beam's upper end, and I_0 and I_1 are the moments of inertia of the spinner. In particular, we assume that the gyroscopic spinner is a solid of revolution, for which I_1 is the moment of inertia about the axis of revolution, and I_0 is the moment of inertia about the transverse principal axes passing through the base of the spinner. We note that the base of the spinner coincides with the upper end of the beam and is located at $z = L$. The quantity Ω, referred to as *gyricity*, is given by [15, 16]

$$\Omega = \dot{\phi} + \dot{\psi} = \mathrm{Const}\,, \tag{6}$$

where $\dot{\phi}$ and $\dot{\psi}$ are the precession and spin rates, respectively. The gyricity is maintained constant throughout the motion, as derived analytically in Section 3 of [15].

We also require junction conditions, which describe the coupling between the elastic beam and the thin elastic plate. These conditions are

$$\boldsymbol{\mathcal{V}}_\mathrm{b}(0) = \mathbf{0}\,, \tag{7}$$

$$E_{\rm b}J_{\rm b}\boldsymbol{\mathcal{V}}_{\rm b}''(0) = -\frac{4\pi D(1+\epsilon^2)}{1-\epsilon^2+(1+\epsilon^2)\log(\epsilon)}\boldsymbol{\mathcal{V}}_{\rm b}'(0)\,, \tag{8}$$

$$E_{\rm b}A_{\rm b}W_{\rm b}'(0) = \frac{16\pi D(1-\epsilon^2)}{R^2\left[(1-\epsilon^2)^2-4\epsilon^2\log^2(\epsilon)\right]}W_{\rm b}(0)\,, \tag{9}$$

where $\epsilon = a/R$. The derivation of (8) and (9) will be given in Section 2.1. The junction conditions (8) correspond to a "logarithmic rotational spring", as discussed below, and represent the relations between bending moments and rotations in the beam at the junction with the plate. The junction condition (9) shows how the axial force in the beam depends on the displacement at the junction with the plate. In the model of Kirchhoff plate, the in-plane displacements of the middle plane are zero, as reflected in (7).

2.1. Logarithmic rotational spring

The scope of this section is to derive the junction conditions (8) and (9). To this aim, we consider the model problem of a thin elastic plate of radius R, clamped on the boundary and containing a circular rigid inclusion of radius a centred at the origin. The rigid inclusion mimics well the dynamic behaviour of the Euler-Bernoulli beam at the junction with the plate, since the displacement and rotations of the beam are uniform across its cross-section, analogously to what occurs for a rigid inclusion.

On the boundary of the plate, we impose

$$W_{\rm p}|_{r=R} = \left.\frac{\partial W_{\rm p}}{\partial r}\right|_{r=R} = 0\,. \tag{10}$$

We start by assuming that the inclusion is subjected to a time-harmonic rotation of amplitude Ψ around the y-axis. Accordingly, the conditions on the boundary of the inclusion take the form

$$W_{\rm p}|_{r=a} = -\Psi a\cos(\theta)\,, \quad \left.\frac{\partial W_{\rm p}}{\partial r}\right|_{r=a} = -\Psi\cos(\theta)\,, \tag{11}$$

where r and θ are polar coordinates (see Fig. 2). The displacement in the plate is given by

$$W_{\rm p}(r,\theta) = \left[A_1J_1(\beta_{\rm p}r) + B_1Y_1(\beta_{\rm p}r) + C_1I_1(\beta_{\rm p}r) + D_1K_1(\beta_{\rm p}r)\right]\cos(\theta)\,. \tag{12}$$

Here, $J_n(\cdot)$ and $Y_n(\cdot)$ are the Bessel functions of the first and second kind, respectively, $I_n(\cdot)$ and $K_n(\cdot)$ are the modified Bessel functions of the first and second kind, respectively. The coefficients A_1 through D_1 are obtained by substituting (12) into (10) and (11) and by solving the resulting linear system of equations.

The bending moment M_y, exerted by the plate on the inclusion and acting on a surface whose normal is in the positive y-direction, is given by [48]

$$M_y = \int_0^{2\pi}\left[M_r\cos(\theta) - V_r a\cos(\theta)\right]|_{r=a}\,a\,{\rm d}\theta\,, \tag{13}$$

where

$$M_r = -D\left[\nu_{\rm p}\nabla^2 W_{\rm p} + (1-\nu_{\rm p})\frac{\partial^2 W_{\rm p}}{\partial r^2}\right],$$
$$V_r = -D\left[\frac{\partial}{\partial r}\left(\nabla^2 W_{\rm p}\right) + (1-\nu_{\rm p})\frac{1}{r}\frac{\partial^2}{\partial r\partial\theta}\left(\frac{1}{r}\frac{\partial W_{\rm p}}{\partial\theta}\right)\right]. \tag{14}$$

In the static limit, when $\beta_{\rm p} \to 0$, the bending moment takes the form

$$M_y^{\rm static} = \lim_{\beta_{\rm p}\to 0} M_y = \frac{4\pi D(1+a^2/R^2)}{1-a^2/R^2+(1+a^2/R^2)\log(a/R)}\Psi\,. \tag{15}$$

A similar relation can be found for the bending moment M_x and the rotation about the x-axis. This completes the derivation of (8). We note that the bending moment M_y generates a negative curvature in the beam, here represented by the rigid inclusion. Accordingly, we have introduced a minus sign on the right-hand side of (8).

Now we assume that the rigid inclusion is subjected to a time-harmonic displacement of constant amplitude Z. In this case, the displacement field in the plate has to satisfy the following boundary conditions:

$$W_{\rm p}|_{r=a} = Z\,, \quad \left.\frac{\partial W_{\rm p}}{\partial r}\right|_{r=a} = 0\,. \tag{16}$$

Hence, the displacement field is axisymmetric and has the form

$$W_{\rm p}(r) = A_0 J_0(\beta_{\rm p} r) + B_0 Y_0(\beta_{\rm p} r) + C_0 I_0(\beta_{\rm p} r) + D_0 K_0(\beta_{\rm p} r)\,. \tag{17}$$

The coefficients A_0 through D_0 are determined from the boundary conditions (10) and (16).

The shear force V_z, exerted by the plate on the inclusion and acting in the positive z-direction, is given by [48]

$$V_z = \int_0^{2\pi} V_r|_{r=a}\, a\,{\rm d}\theta\,. \tag{18}$$

In the static limit, when $\beta_{\rm p} \to 0$, it takes the form

$$V_z^{\rm static} = \lim_{\beta_{\rm p}\to 0} V_z = \frac{16\pi D(a^2-R^2)}{(a^2-R^2)^2 - 4a^2R^2\log^2(a/R)}Z\,, \tag{19}$$

which completes the derivation of (9). We point out that the force V_z acts as a compressive force for the beam, represented here by the inclusion. This has been taken into account by changing the sign of the the right-hand side of (9).

2.2. Eigenfrequencies as functions of gyricity

Here, we determine the eigenfrequencies of the chiral system in Fig. 2 by solving the eigenvalue problem (3)-(9). For simplicity, we assume that the inertia of the plate and beam is negligibly small compared with the mass of the

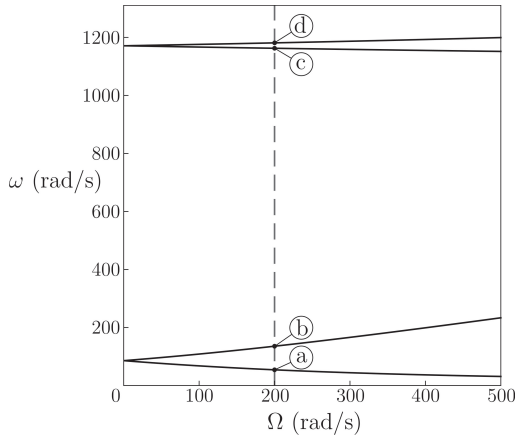

Figure 3: Eigenfrequencies corresponding to the flexural motion of the chiral multi-structure in Fig. 2 versus the gyricity Ω. The frequencies $\omega_{\rm a}$, $\omega_{\rm b}$, $\omega_{\rm c}$ and $\omega_{\rm d}$ are computed for $\Omega = 200$ rad/s.

gyroscopic spinner ($\rho_{\rm p}, \rho_{\rm b} \to 0$). As a consequence, the number of eigenfrequencies of the system is finite.

For the numerical calculations, we set the parameters as follows: for the plate $E_{\rm p} = 70$ GPa, $\nu_{\rm p} = 0.3$, $h = 0.01$ m, $R = 1$ m; for the beam $E_{\rm b} = 70$ GPa, $L = 1$ m, $a = 0.05$ m; for the gyroscopic spinner $m = 1$ kg, $I_0 = 4$ kg m^2, $I_1 = 2$ kg m^2, $c = 0$, $l = 0.1$ m. The eigenfrequencies ω of the system associated with its flexural motion depend on the gyricity Ω, as shown in Fig. 3. When $\Omega = 0$, which corresponds to the case when the spinner behaves like a rigid body with translational and rotational inertia, two double eigenfrequencies are identified; when $\Omega > 0$, the gyricity leads to a splitting of the double eigenfrequencies.

When $\Omega = 200$ rad/s (dashed line in Fig. 3), the eigenfrequencies determined analytically from the eigenvalue problem (3)-(9) are given by $\omega_{\rm a} = 54.2$ rad/s, $\omega_{\rm b} = 135.5$ rad/s, $\omega_{\rm c} = 1162.5$ rad/s, $\omega_{\rm d} = 1181.2$ rad/s. These values are very close to the eigenfrequencies obtained from a finite element model developed in *Comsol Multiphysics* [49], which consists of a one-dimensional Euler-Bernoulli beam attached to a circular clamped plate at one end and with the effective gyroscopic boundary conditions (4) at the other end. The plate is modelled as a (two-dimensional) Kirchhoff plate. The mesh is extremely fine and consists of 82440 triangular elements with quadratic interpolation for the plate and 628 linear elements with cubic interpolation for the beam. The numerical eigenfrequencies are $\omega_{\rm a}^{\rm num} = 53.5$ rad/s, $\omega_{\rm b}^{\rm num} = 134.8$ rad/s, $\omega_{\rm c}^{\rm num} = 1161.1$ rad/s, $\omega_{\rm d}^{\rm num} = 1179.8$ rad/s. The eigenmodes of the system corresponding to the four eigenfrequencies above are illustrated in Videos 1a-1d, included in the Supplementary Material accompanying this paper.

The diagram in Fig. 3, showing how the natural frequency ω varies with the gyricity Ω, is similar to the dependence of the natural frequencies of a rotating shaft on its spin speed [50]. This behaviour has also been observed in

rods connected to spinning tip rotors [51] and in the dynamics of gyroelastic continua [17]. We point out that the first eigenfrequency of the system tends to zero in the limit when $\Omega \to \infty$. Hence, in the system under consideration there is no zero natural frequency for a finite value of gyricity, associated with instabilities observed in other types of rotating systems. In this paper, our main focus is on the preferential directionality associated with each branch of the diagram in Fig. 3 (see Videos 1a-1d), which makes the flexural waves chiral and will be used to generate one-way wave propagation in Section 4.

The eigenfrequency associated with the axisymmetric motion of the multi-structure, which does not depend on the gyricity Ω, is equal to $\omega_{\rm e} = 595.7$ rad/s. This value is in good agreement with the numerical outcomes from the same simulation in *Comsol Multiphysics*, which provides $\omega_{\rm e}^{\rm num} = 594.3$ rad/s. The corresponding eigenmode is shown in Video 1e of the Supplementary Material.

In order to show the effect of non-zero density in the plate and beam, we have performed numerical simulations in *Comsol Multiphysics* where the density of the plate and the beam is taken as $\rho_{\rm p} = \rho_{\rm b} = 2700$ kg/m^3. Fig. SM1 in the Supplementary Material shows how in this case the eigenfrequencies ω vary with the gyricity Ω. We note that the effect of the gyroscopic spinner is similar to that observed in Fig. 3, namely, adding the gyricity Ω splits the double eigenfrequencies determined for $\Omega = 0$ into two branches. The presence of non-zero density in the plate and beam moves the curves to lower values of the frequency in comparison with the branches shown in Fig. 3.

2.3. Junction conditions using the Green's function

When the cross-section of the beam is small ($a/R \ll 1$), the junction conditions between the plate and the beam can also be derived using the two-dimensional Green's function.

For a massless circular plate with clamped boundary, the Green's function takes the form [52]

$$G(x,y,\xi,\eta) = \frac{1}{8\pi D}\left\{\frac{1}{2R^2}\left[R^2-(x^2+y^2)\right]\left[R^2-(\xi^2+\eta^2)\right] - \left[(x-\xi)^2+(y-\eta)^2\right]\log\left[\frac{\sqrt{(R^2-x\xi-y\eta)^2+(y\xi-x\eta)^2}}{R\sqrt{(x-\xi)^2+(y-\eta)^2}}\right]\right\}, \tag{20}$$

where (ξ,η) is the point of application of the unit force.

Consider a pair of force couples, separated by small distances $2\epsilon_y$ and $2\epsilon_x$ along the y- and x-axes, respectively. The corresponding displacement fields have the form

$$\mu_x = \frac{1}{2\epsilon_y}\left[G(x,\epsilon_y,\xi,\eta) - G(x,-\epsilon_y,\xi,\eta)\right] \tag{21}$$

and

$$\mu_y = \frac{1}{2\epsilon_x}\left[G(\epsilon_x,y,\xi,\eta) - G(-\epsilon_x,y,\xi,\eta)\right], \tag{22}$$

respectively. We note that

$$\mu_x \to \frac{\partial G}{\partial y} \text{ when } \epsilon_y \to 0\,, \quad \mu_y \to \frac{\partial G}{\partial x} \text{ when } \epsilon_x \to 0\,. \tag{23}$$

Consequently, the rotations corresponding to the moments around the x- and y-axes are

$$\phi_x = \frac{\partial^2 G}{\partial y^2}\,, \quad \phi_y = \frac{\partial^2 G}{\partial x^2}\,. \tag{24}$$

When the a/R is small, we obtain

$$\begin{aligned} &\lim_{(x,y)\to(0,0)} G(x,y,0,0) = \frac{R^2}{16\pi D}\,, \\ &\lim_{(x,y)\to(0,0)} \phi_x(x,y,0,0) = \lim_{(x,y)\to(0,0)} \phi_y(x,y,0,0) = \frac{\log(a/R)}{4\pi D}\,. \end{aligned} \tag{25}$$

Using (25) and taking into account the sign convention adopted for the bending moments and axial force in the beam, the junction conditions between the beam and the plate in the limit when $a/R \to 0$ can be written as

$$E_{\rm b} J_{\rm b} \boldsymbol{\mathcal{V}}_{\rm b}''(0) = -\frac{4\pi D}{\log(a/R)} \boldsymbol{\mathcal{V}}_{\rm b}'(0)\,, \tag{26}$$

and

$$E_{\rm b} A_{\rm b} W_{\rm b}'(0) = \frac{16\pi D}{R^2} W_{\rm b}(0)\,. \tag{27}$$

Eqs. (26) and (27) coincide with (8) and (9) in the limit when $a/R \to 0$.

The Green's function (20) and the procedure described in this section are very useful, since they can be applied to the case when the beam is attached to any point in the interior of the plate.

The effect of the boundary of the plate decreases as $a/R \to 0$. Accordingly, the Green's function approach can be employed for the case when the plate has different boundary conditions or a different shape or when the cross-section of the beam is not circular.

3. Periodic system of chiral resonators on a flexural foundation

Here, we study propagation of Bloch-Floquet elastic waves of radian frequency ω in the periodic structure (shown in Fig. 4), composed of a two-dimensional periodic array of beams attached to an infinite Kirchhoff plate. At the top end of each beam, a gyroscopic spinner is connected in the same way as described in Section 2. The cross-section of each beam is circular and has radius a. The elementary cell of the periodic structure, highlighted in grey in Fig. 4, is a rectangle with side lengths d_x and d_y, where $d_y = \sqrt{3} d_x$. The position vectors of the resonators in the xy-plane are defined by $\boldsymbol{r}_{nm} = (nd_x, md_y)$, where n and m are integers. We also assume that $a \ll d_x$. The singular perturbation for a

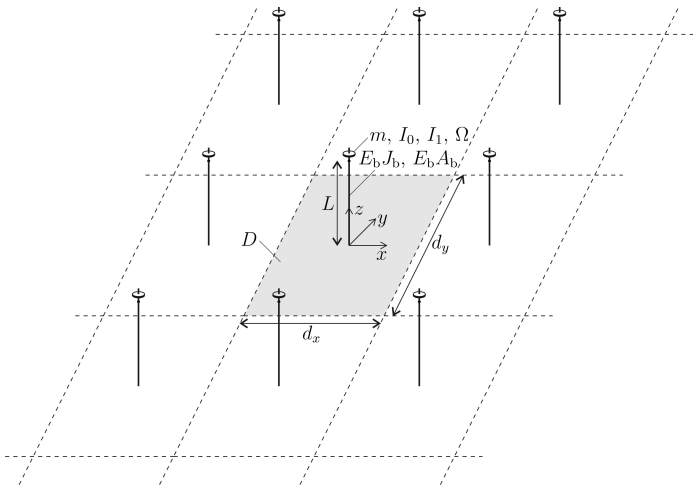

Figure 4: Two-dimensional array of chiral resonators on an infinite thin plate. The resonators consist of Euler-Bernoulli beams connected to gyroscopic spinners at their tips. The elementary cell of the periodic system is highlighted.

circular plate developed in Section 2.1, leading to the junction conditions (8) and (9), cannot be employed here, since the elementary cell has a rectangular shape. Instead, since $a \ll d_x$, the approach based on the Green's function outlined in Section 2.3 will be used (see system (A.2) in the Appendix). As in Section 2, we assume that the inertia of the system is concentrated at the gyroscopic spinners.

Within the elementary cell, $\boldsymbol{x} \in (-d_x/2, d_x/2) \times (-d_y/2, d_y/2)$, the flexural displacement of the plate satisfies

$$D\Delta^2 W_\mathrm{p} - N_z(0)\delta(\boldsymbol{x}) + M_x(0)\frac{\partial}{\partial y}\delta(\boldsymbol{x}) - M_y(0)\frac{\partial}{\partial x}\delta(\boldsymbol{x}) = 0\,, \tag{28}$$

where $N_z(z)$, $M_x(z)$ and $M_y(z)$ are the axial force and bending moments transmitted by the beam. Appropriate quasi-periodicity conditions are imposed on the transverse displacement, namely

$$W_\mathrm{p}\left(x + nd_x, y + md_y\right) = W_\mathrm{p}\left(x, y\right)\mathrm{e}^{i(k_x n d_x + k_y m d_y)}\,, \tag{29}$$

and on its derivatives. Here, $\boldsymbol{k} = (k_x, k_y)^\mathrm{T}$ is the Bloch vector.

The axial force and bending moments transmitted by the beam to the plate can be written as $N_z(0) = \mathscr{N}\delta_z$, $M_x(0) = \mathscr{M}_1\alpha_x + \mathscr{M}_2\alpha_y$ and $M_y(0) = -\mathscr{M}_2\alpha_x + \mathscr{M}_1\alpha_y$, respectively, where δ_z is the displacement and α_x, α_y are the rotations at the base of the beam. The displacement and rotations are uniform on the beam cross-section. The expressions for the quantities $\mathscr{N}$, $\mathscr{M}_1$ and $\mathscr{M}_2$ are derived in Section 3.1 (see Eqs. (33) and (31)).

The dispersion diagram of the periodic system is discussed in Section 3.2.

3.1. The axial force and bending moments at the base of the beam

In this section, we derive the axial force and bending moments at the base of each beam. In this way, the beams can be removed from the formulation and their effect can be reproduced by effective axial force and bending moments in the plate. To this aim, we consider the model problem of a massless Euler-Bernoulli beam of length L, flexural stiffness $E_\mathrm{b}J_\mathrm{b}$ and axial stiffness $E_\mathrm{b}A_\mathrm{b}$. The reference system is shown in Fig. 4, where z is the longitudinal coordinate and x and y are the transverse coordinates with respect to the beam axis. At $z = L$ a gyroscopic spinner is attached to the beam, while at $z = 0$ the beam has prescribed displacements and rotations.

From (3) with $\rho_\mathrm{b} = 0$, we find that the transverse displacement amplitudes U_b and V_b are cubic functions of z, while the longitudinal displacement amplitude W_b is a linear function of z. The ten coefficients defining the functions U_b, V_b and W_b are determined by solving the system consisting of the five boundary conditions (4) at $z = L$ (where we take $c = 0$ as in Section 2) and the five boundary conditions at $z = 0$, given by (7) and by $U_\mathrm{b}'(0) = \alpha_y$, $V_\mathrm{b}'(0) = \alpha_x$ and $W_\mathrm{b}(0) = \delta_z$. We find that the amplitudes of the displacement components are then given by

$$\begin{aligned}
U_\mathrm{b}(z) &= \left(\frac{\mathscr{N}_1}{\mathscr{D}}\alpha_x + \frac{\mathscr{N}_2}{\mathscr{D}}\alpha_y\right) z^3 + \left(-\frac{\mathscr{N}_3}{\mathscr{D}}\alpha_x + \frac{\mathscr{N}_4}{\mathscr{D}}\alpha_y\right) z^2 + \alpha_y z\,, \\
V_\mathrm{b}(z) &= \left(\frac{\mathscr{N}_2}{\mathscr{D}}\alpha_x - \frac{\mathscr{N}_1}{\mathscr{D}}\alpha_y\right) z^3 + \left(\frac{\mathscr{N}_4}{\mathscr{D}}\alpha_x + \frac{\mathscr{N}_3}{\mathscr{D}}\alpha_y\right) z^2 + \alpha_x z\,, \\
W_\mathrm{b}(z) &= \left(\frac{m\omega^2}{E_\mathrm{b}A_\mathrm{b} - ml\omega^2} z + 1\right) \delta_z\,,
\end{aligned} \tag{30}$$

where

$$\begin{aligned}
\mathscr{N}_1 &= 2\mathrm{i}E_\mathrm{b}J_\mathrm{b}mI_1l^2\Omega\omega^3\left(6E_\mathrm{b}J_\mathrm{b} + ml^3\omega^2\right)\,, \\
\mathscr{N}_2 &= ml\omega^2\left(I_0l\omega^2 - 2E_\mathrm{b}J_\mathrm{b}\right)\left[12(E_\mathrm{b}J_\mathrm{b})^2 - 4E_\mathrm{b}J_\mathrm{b}l\left(3I_0 + ml^2\right)\omega^2 + mI_0l^4\omega^4\right] \\
&\quad + ml^3I_1^2\Omega^2\omega^4\left(12E_\mathrm{b}J_\mathrm{b} - ml^3\omega^2\right)\,, \\
\mathscr{N}_3 &= 2\mathrm{i}E_\mathrm{b}J_\mathrm{b}I_1\Omega\omega\left(6E_\mathrm{b}J_\mathrm{b} + ml^3\omega^2\right)^2\,, \\
\mathscr{N}_4 &= 2\omega^2\left\{36(E_\mathrm{b}J_\mathrm{b})^3\left(ml^2 + I_0\right) + E_\mathrm{b}J_\mathrm{b}ml^4\omega^2\left[I_0\left(15I_0 + 7ml^2\right)\omega^2 - 15I_1^2\Omega^2\right]\right. \\
&\quad \left. + m^2l^7\omega^4\left(I_1^2\Omega^2 - I_0^2\omega^2\right) + 12(E_\mathrm{b}J_\mathrm{b})^2l\left[3I_1^2\Omega^2 - \left(3I_0^2 + 5mI_0l^2 + m^2l^4\right)\omega^2\right]\right\}\,, \\
\mathscr{D} &= \left[12(E_\mathrm{b}J_\mathrm{b})^2 - 4E_\mathrm{b}J_\mathrm{b}l\left(3I_0 + ml^2\right)\omega^2 + mI_0l^4\omega^4\right]^2 \\
&\quad - I_1^2l^2\Omega^2\omega^2\left(12E_\mathrm{b}J_\mathrm{b} - ml^3\omega^2\right)^2\,.
\end{aligned} \tag{31}$$

The bending moments and axial force at the base of the beam have the form

$$\begin{aligned}
M_x(0) &= -E_\mathrm{b}J_\mathrm{b}V_\mathrm{b}''(0) = \mathscr{M}_1\alpha_x + \mathscr{M}_2\alpha_y\,, \\
M_y(0) &= -E_\mathrm{b}J_\mathrm{b}U_\mathrm{b}''(0) = -\mathscr{M}_2\alpha_x + \mathscr{M}_1\alpha_y\,, \\
N_z(0) &= E_\mathrm{b}A_\mathrm{b}W_\mathrm{b}'(0) = \mathscr{N}\delta_z\,,
\end{aligned} \tag{32}$$

where

$$\begin{aligned}\mathscr{M}_1 &= -\frac{2E_\mathrm{b}J_\mathrm{b}\mathscr{N}_4}{\mathscr{D}}\,,\\ \mathscr{M}_2 &= -\frac{2E_\mathrm{b}J_\mathrm{b}\mathscr{N}_3}{\mathscr{D}}\,,\\ \mathscr{N} &= \frac{E_\mathrm{b}A_\mathrm{b}m\omega^2}{E_\mathrm{b}A_\mathrm{b}-ml\omega^2}\,.\end{aligned} \tag{33}$$

3.2. Dispersion of chiral Bloch-Floquet waves

Since the inertia distribution is discrete, we expect the system to exhibit a finite number of dispersion surfaces. The solid grey lines in Fig. 5a represent the complete band diagram of the system with chiral resonators, obtained by employing the regularisation procedure described in the Appendix. The diagram is calculated in the reciprocal lattice space along the path $\Gamma\,\mathrm{X}\,\mathrm{M}\,\mathrm{Y}\,\Gamma$, presented in Fig. 5b.

The results of Fig. 5 are obtained for a plate with elastic modulus $E_\mathrm{p} = 70$ GPa, Poisson's ratio $\nu_\mathrm{p} = 0.3$, thickness $h = 0.01$ m, and side lengths $d_x = 2$ m and $d_y = 2\sqrt{3}$ m. The beam has Young's modulus $E_\mathrm{b} = 70$ GPa, length $L = 1$ m and circular cross-section with radius $a = 0.02$ m. The gyroscopic spinner is characterised by the mass $m = 1$ kg, moments of inertia $I_0 = 4$ kg m^2 and $I_1 = 2$ kg m^2, length $l = 0.1$ m and gyricity $\Omega = 200$ rad/s.

In order to validate the analytical procedure developed in the Appendix, we have compared the analytical results with the numerical outcomes obtained from an independent finite element model built in *Comsol Multiphysics* [49]. The geometry used in the computations consists of a rectangular plate with sides d_x and $d_y = \sqrt{3}d_x$ and a beam element, with one end attached to the centre of the plate. As in Section 2.2, the plate is modelled as a (two-dimensional) Kirchhoff plate and the rod as a (one-dimensional) Euler-Bernoulli beam. In the finite element model the singular perturbation approach is not used, and the connection between the plate and the beam incorporates continuity of displacements and rotations. The gyroscopic boundary conditions (4) are imposed on the other end of the beam. The extremely fine mesh is made of 40422 triangular elements with quadratic interpolation for the plate and 548 linear elements with cubic interpolation for the beam. In addition, Bloch-Floquet conditions are applied

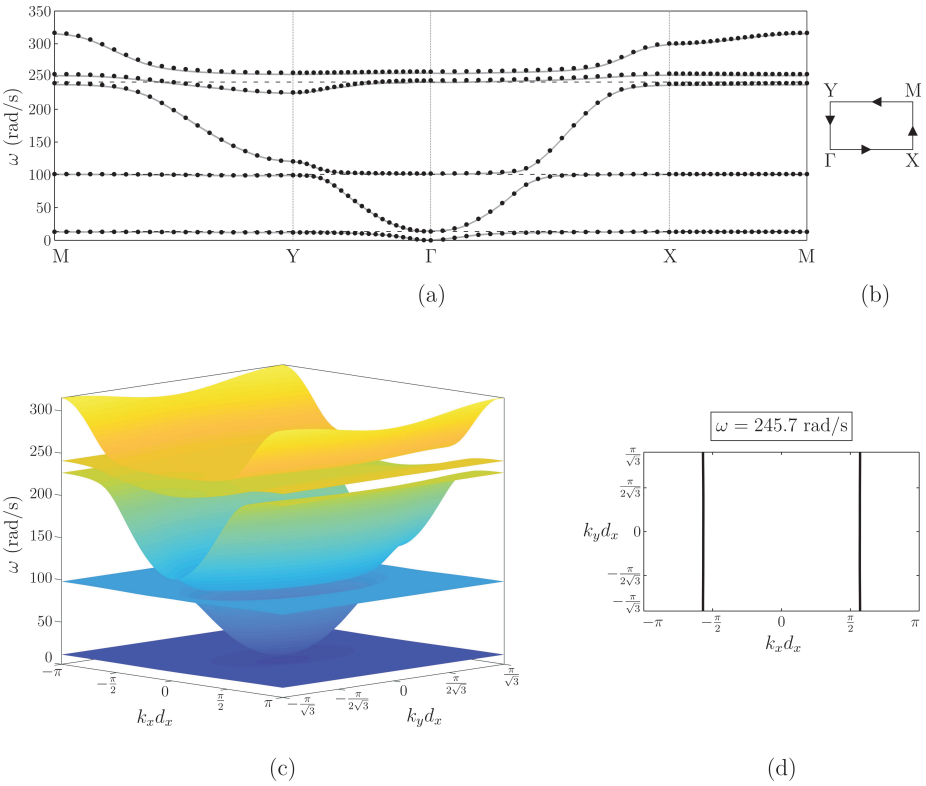

Figure 5: (a) Band diagram of the periodic system in Fig. 4 with $\Omega = 200$ rad/s, evaluated along the path $\Gamma\,\mathrm{X}\,\mathrm{M}\,\mathrm{Y}\,\Gamma$ shown in (b). Analytical (solid grey lines) and numerical (black dots) results are compared. The dashed horizontal lines indicate the frequencies that will be used in the numerical simulations of Section 4. (c) Dispersion surfaces of the system, determined numerically. (d) Slowness contours calculated for $\omega = 245.7$ rad/s.

on the boundaries of the elementary cell:

$$
\begin{aligned}
&W_{\mathrm{p}}|_{x=d_x/2} = W_{\mathrm{p}}|_{x=-d_x/2}\,\mathrm{e}^{ik_x d_x}\,, \quad \left.\frac{\partial W_{\mathrm{p}}}{\partial y}\right|_{x=d_x/2} = \left.\frac{\partial W_{\mathrm{p}}}{\partial y}\right|_{x=-d_x/2}\mathrm{e}^{ik_x d_x}\,,\\
&M_{xx}|_{x=d_x/2} = M_{xx}|_{x=-d_x/2}\,\mathrm{e}^{ik_x d_x}\,, \quad M_{xy}|_{x=d_x/2} = M_{xy}|_{x=-d_x/2}\,\mathrm{e}^{ik_x d_x}\,,\\
&V_x|_{x=d_x/2} = V_x|_{x=-d_x/2}\,\mathrm{e}^{ik_x d_x}\,,\\
&W_{\mathrm{p}}|_{y=d_y/2} = W_{\mathrm{p}}|_{y=-d_y/2}\,\mathrm{e}^{ik_y d_y}\,, \quad \left.\frac{\partial W_{\mathrm{p}}}{\partial x}\right|_{y=d_y/2} = \left.\frac{\partial W_{\mathrm{p}}}{\partial x}\right|_{y=-d_y/2}\mathrm{e}^{ik_y d_y}\,,\\
&M_{yy}|_{y=d_y/2} = M_{yy}|_{y=-d_y/2}\,\mathrm{e}^{ik_y d_y}\,, \quad M_{yx}|_{y=d_y/2} = M_{yx}|_{y=-d_y/2}\,\mathrm{e}^{ik_y d_y}\,,\\
&V_y|_{y=d_y/2} = V_y|_{y=-d_y/2}\,\mathrm{e}^{ik_y d_y}\,,
\end{aligned}
\tag{34}
$$

where $M_{xx} = -D(W_{\mathrm{p},xx} + \nu W_{\mathrm{p},yy})$, $M_{yy} = -D(W_{\mathrm{p},yy} + \nu W_{\mathrm{p},xx})$, $M_{xy} = M_{yx} = -D(1-\nu)W_{\mathrm{p},xy}$ represent the moments and $V_x = M_{xx,x} + M_{xy,y}$, $V_y = M_{yy,y} + M_{yx,x}$ denote the shear forces.

The dispersion diagram is computed by solving the eigenvalue problem for the system for different values of the wave vector. We remark that the mesh for the plate needs to be extremely fine, especially in the surrounding vicinity of the connection with the beam. The numerical findings are indicated by black dots in Fig. 5a. It can be seen that the agreement with the analytical results is excellent.

The dispersion surfaces of the system, determined using the finite element model in *Comsol Multiphysics*, are plotted in Fig. 5c. Parabolic modes are identified at specific frequencies. For example, the slowness contours at $\omega = 245.7$ rad/s are presented in Fig. 5d. Since the contour lines are approximately parallel to the k_y-axis in the reciprocal space, waves at that frequency are forced to propagate in the x-direction in the physical space. Examples of this type of parabolic modes will be discussed in Section 4.

The limits of the stop-bands in Figs. 5a and 5c can be determined analytically. In particular, the frequencies of standing waves for $\boldsymbol{k} = \boldsymbol{0}$ are very close to the flexural eigenfrequencies of the finite system examined in Section 2, consisting of a clamped circular plate and an elastic beam, connected to the centre of the plate at its lower end and to a gyroscopic spinner at its upper end (see Fig. 2). Taking the radius of the circular plate equal to the semi-diagonal of the rectangular elementary cell (i.e. $R = \sqrt{d_x^2 + d_y^2}/2$), we obtain the following eigenfrequencies of the finite system associated with flexural motion: $\omega = 13.71$, 102.49, 247.79, 259.01 rad/s. These values are very close to the limits of the stop-bands for $\boldsymbol{k} = \boldsymbol{0}$, given by $\omega = 13.53$, 101.96, 244.11, 257.39 rad/s.

We point out that in the limit when the radius of the circular plate tends to infinity, the flexural eigenfrequencies of the multi-structure in Fig. 2 coincide with those of a beam with a hinge at the lower end and a gyroscopic spinner at the upper end, analysed in [53]. This can be explained on physical grounds

considering that when $R \to \infty$ the junction condition degenerates to a hinge, with zero moments. Any rotation of the beam at the junction point is admissible when $\epsilon = a/R \to 0$ in (8). Using the analytical formulation in [53] or solving the eigenvalue problem described in Section 2 of the present paper, we find that the flexural eigenfrequencies when $R \to \infty$ are given by $\omega = 0$, 75.78, 174.89, 199.11 rad/s.

When $\Omega = 0$, the gyroscopic spinners behave as rigid bodies with translational mass m and moment of inertia I_0 about the x- and y-axes. For this case, the band diagram along the edges of the Brillouin zone and the dispersion surfaces of the system are shown in Figs. 6a and 6c, respectively. Comparing Figs. 5 and 6, we note that the main effect of increasing gyricity is to lower the first stop-band and to move the second one upwards. Furthermore, it is observed that with increasing gyricity the widths of the two lowest stop-bands increase. At higher frequencies, the effect of gyricity on the dispersion surfaces is less pronounced. In particular, we notice that the upper pass-bands are slightly lifted up. As in the case $\Omega \neq 0$, it is possible to identify frequencies at which parabolic modes are generated, such as $\omega = 247.1$ rad/s (see Fig. 6d).

For completeness, in Figs. SM2 and SM3 of the Supplementary Material we show how the dispersion diagrams change as different values of the gyricity Ω are considered.

4. Forced problem: one-way unidirectional waves in the chiral flexural system

In this section, we study the motion of a finite system under time-harmonic loading. The system, shown in Fig. 7, consists of a thin plate with a 50×30 array of chiral resonators. The elementary cell of this system is identical to that illustrated in Fig. 4 and the parameters are the same as considered in Section 3. The domain is divided into two regions: in the lower region the gyricity $\Omega = 200$ rad/s, while in the upper one $\Omega = -200$ rad/s. The dispersion diagrams of the corresponding periodic structure are the same for both values of Ω and they are shown in Fig. 5. The system is subjected to a time-harmonic force, applied to the tip of a beam in a cell close to the interface and located in the lower region where the gyricity is positive (see Fig. 7). The force induces a gyroscopic force on the beam, which transmits bending moments to the plate with respect to both the x- and y-axes. In order to reduce the effect of the reflected waves from the boundaries, *Perfectly Matched Layers* (PML) are introduced into the model. The extent of PML is indicated by the grey dashed lines in Fig. 7. In the numerical computations, PML are modelled as plate elements with damping. The parameters of the PML have been optimised in order to minimise the amplitudes of the waves reflected by the boundaries. We remark that PML are frequency dependent.

The interface between the two domains, with equal and opposite values of gyricity, is a line parallel to the x-axis (see dot-dashed line in Fig. 7). The reason for this choice of the interface is due to the fact that waves tend to

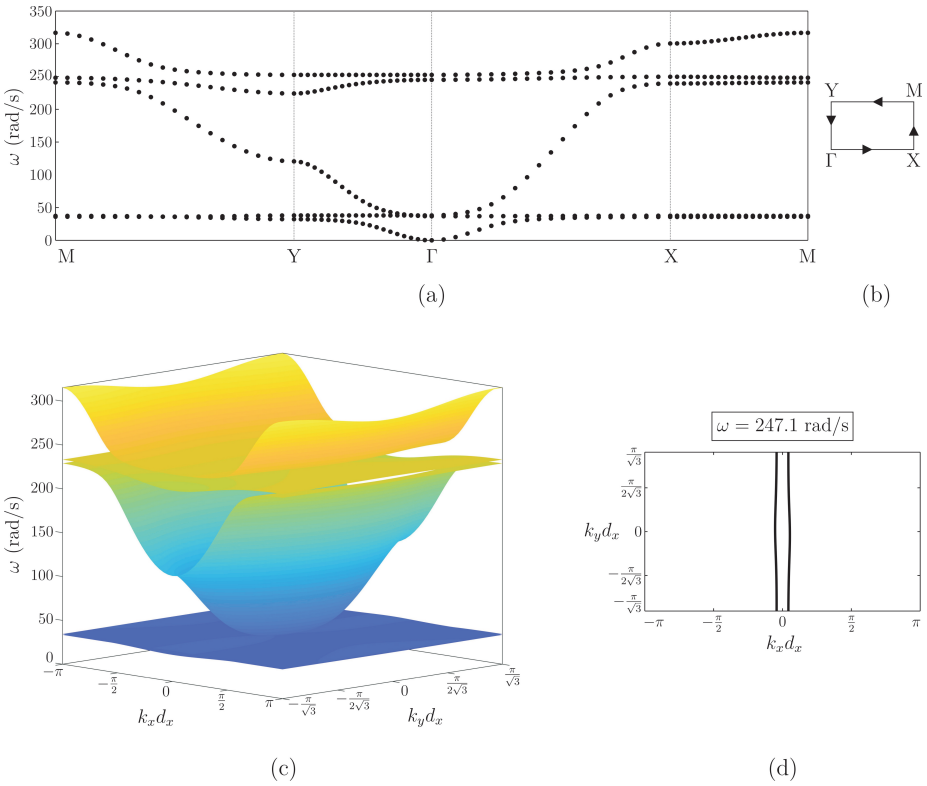

Figure 6: (a) Band diagram of the periodic system in Fig. 4 with $\Omega = 0$, calculated along the path Γ X M Y Γ illustrated in (b). (c) Dispersion surfaces of the system, computed numerically. (d) Slowness contours for $\omega = 247.1$ rad/s.

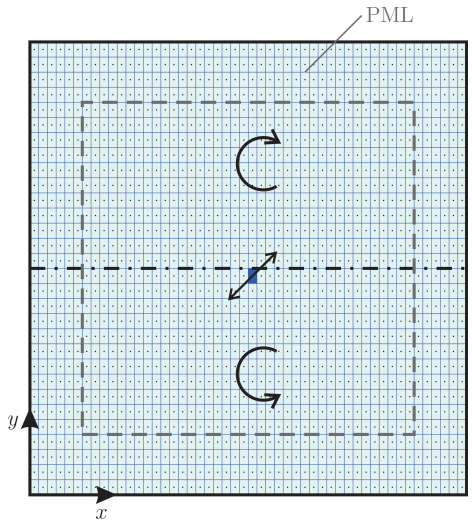

Figure 7: A two-dimensional finite array of cells, one of which is highlighted in grey in Fig. 4. The gyricity $\Omega = 200$ rad/s below the dot-dashed line, while $\Omega = -200$ rad/s above the dot-dashed line. A time-harmonic force is applied at the top of a beam, in the position and direction indicated by the arrow. PML are inserted near the edges of the domain to absorb impinging waves.

propagate in the x-direction at certain frequencies, as shown by the slowness contours in Fig. 5d.

One-way unidirectional waves are connected to the chiral response of the elastic system. Chirality also influences the eigenmodes of the periodic structure, where flexural vibrations are coupled with rotational motion. The direction of rotation changes with the frequency and the wave vector. For the same values of the frequency and wave vector, the direction of rotation is changed if the sign of gyricity is changed. Accordingly, in the model of Fig. 7 we expect that at some special frequencies waves propagate only in one direction.

In Fig. 8a we show the displacement amplitude W_{p} in the plate calculated for an angular frequency of the time-harmonic forcing of 13.0 rad/s. This frequency is inside the first stop-band of the infinite system (see lowest dashed line in Fig. 5a). In the numerical computations, the amplitude of the force is equal to 1 N. As is apparent from the figure, waves propagate along the interface to the left of the force, before being dissipated inside the PML. To the right of the force, the displacements are negligibly small.

Another example of a one-way unidirectional wave was presented in the Introduction (see Fig. 1). There, the radian frequency is 101.5 rad/s. This frequency lies in the second stop-band of the infinite system (refer to Fig. 5a). In this situation, the wave propagates in the opposite direction to that considered in Fig. 8a.

The examples in Figs. 1 and 8a show that the direction of wave propagation depends on the stop-band in which we choose the frequency of excitation. The

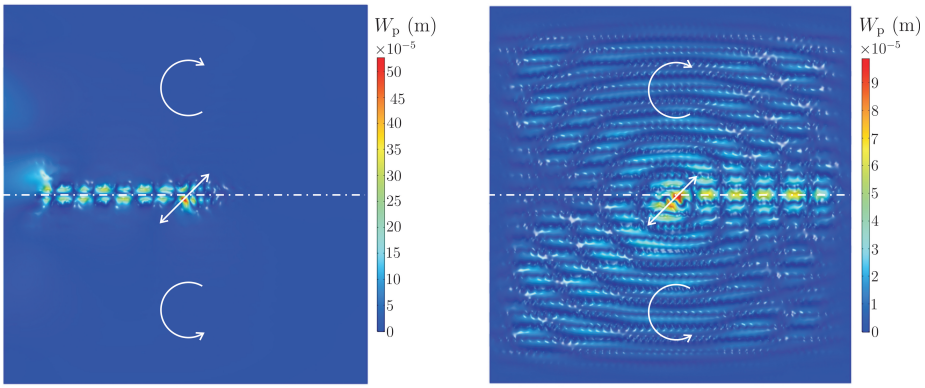

(a) (b)

Figure 8: Displacement amplitude field in the chiral flexural structure of Fig. 7, generated by a time-harmonic force of amplitude 1 N and radian frequency (a) $\omega = 13.0$ rad/s and (b) $\omega = 244.7$ rad/s.

direction of wave propagation can be predicted by looking at the eigenfunctions of the elementary cell, evaluated for a given wave vector at an eigenfrequency below and above the band-gap where the frequency of excitation is chosen. In particular, considering the configuration in Figure 7 and for this particular set of parameter values, if below the chosen band-gap the beam in the elementary cell rotates clockwise and above the band-gap the beam rotates counter-clockwise, the wave generated by the excitation travels to the left of the point of application of the force, as in Fig. 8a. Conversely, if at an eigenfrequency below (above) the band-gap the beam rotates in the counter-clockwise (clockwise) direction, the wave propagates to the right of the force, as in Fig. 1.

In Figs. 1 and 8a the frequencies of excitation are inside the stop-bands of the corresponding infinite system. Conversely, Fig. 8b shows the displacement amplitude field when the force has a radian frequency of 244.7 rad/s, falling inside a high-frequency pass-band (see highest dashed line in Fig. 5a). In this case, the system response shows a preferential directionality to the right of the force, where most of the energy is transmitted. However, there is also a wave of small amplitude propagating in the y-direction, both upwards and downwards, since the frequency lies in a partial stop-band.

In all these numerical computations, the direction of the force is at 45° with respect to the x-axis. However, the direction of the force does not affect the results significantly, because the chiral terms in the boundary conditions (4) couple the transverse displacement components of the beam. Consequently, a force in one direction would generate displacements in both the parallel and perpendicular directions.

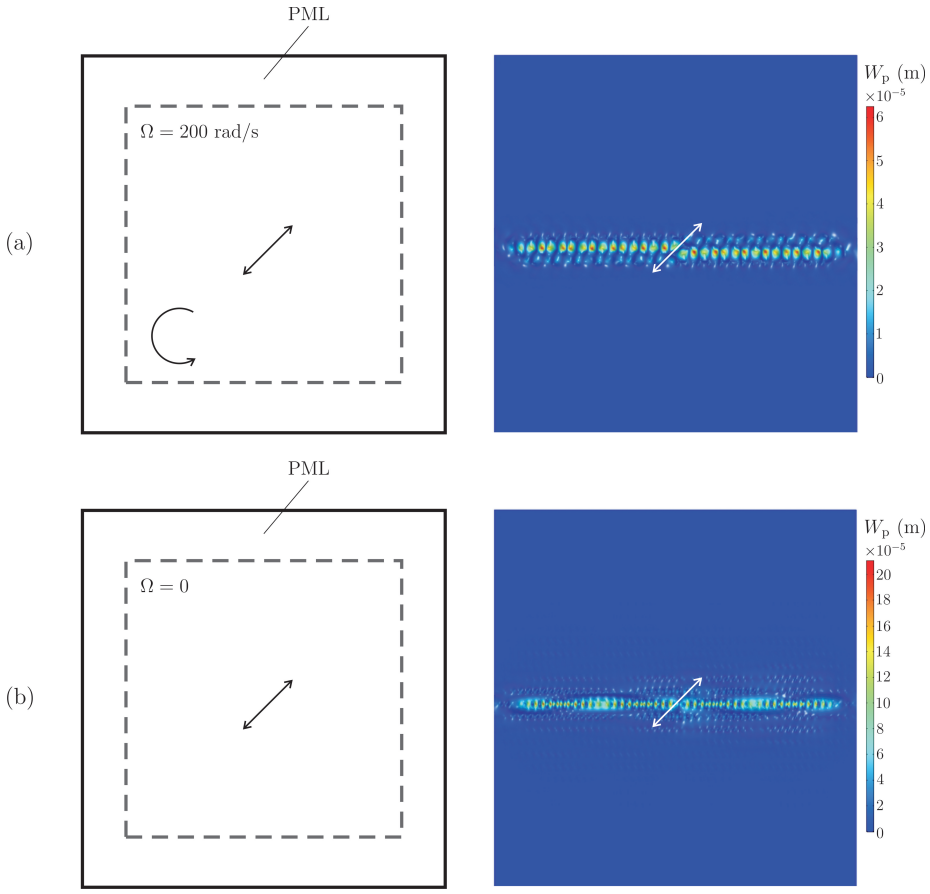

Figure 9: Time-harmonic response of the uniform chiral flexural structure to a force of amplitude 1 N and radian frequency (a) $\omega = 245.7$ rad/s and (b) $\omega = 247.1$ rad/s. The value of the gyricity Ω in each case is indicated in the figures.

5. Forced problem: localised waveforms in a structure with uniform gyricity

In this section, we study the dynamic response of the flexural chiral system to an external excitation, where the gyricity of the spinners is uniform throughout the structure. The value of the gyricity is assumed to be either $\Omega = 200$ rad/s or $\Omega = 0$; the other parameters are the same as those considered in Section 3.

Fig. 9a shows the flexural displacement amplitude field in the plate when $\Omega = 200$ rad/s and the radian frequency is $\omega = 245.7$ rad/s. It is apparent that waves propagate along the x-axis, both to the left and to the right of the point of application of the force. The waveform generated by the force is highly localised. This is consistent with the slowness contours of the corresponding infinite system, presented in Fig. 5d and calculated for the same value of the

radian frequency ω. The slowness contours are parallel straight lines in the reciprocal plane, hence waves can propagate only in the perpendicular direction in the physical plane. Further, this is independent of the orientation of the applied force.

Waveforms localised on a line were also observed in elastic lattices [24, 25]. Here, we have demonstrated that waves propagating along a single line can also be realised in a plate connected to chiral resonators. We emphasise that these parabolic modes do not require an interface separating two sub-domains with different properties. Indeed, the same waveform would be generated along a different horizontal line by moving the force to a different position.

In the case when the gyricity $\Omega = 0$ throughout the structure, we could not detect any frequency at which the slowness contours are parallel straight lines. Nonetheless, quasi-parabolic modes can be generated at specific frequencies, for instance at $\omega = 247.1$ rad/s (see Fig. 6d). In Fig. 9b we illustrate the flexural displacement amplitude field in the structure when the gyricity $\Omega = 0$ and the radian frequency $\omega = 247.1$ rad/s. As expected from the results of the dispersion analysis in the corresponding infinite system, the waveform produced by the force is not as localised as in Fig. 9a, where $\Omega \neq 0$.

6. Conclusions

The present paper has introduced a new class of elastic waveforms, referred to as "chiral flexural waves", for a multi-structure consisting of an elastic plate connected to a system of beams with gyroscopic spinners. The model is based on the novel concept of a "logarithmic junction", which enables us to take into account the coupling between the flexural modes alongside the gyricity of the spinners embedded in the chiral resonators.

The model solutions are written explicitly in the closed analytical form, used in modelling Bloch-Floquet waves in doubly-periodic chiral flexural systems, which have never been analysed in the past. New types of chiral flexural waveforms have been identified. These are not connected with the inertia of the flexural plate, but are entirely produced via the dynamic interaction between chiral elastic resonators.

This novel approach presented here paves the way for the analysis of interfacial waves in a plate along the boundaries of regions of different gyricities, but otherwise uniform elastic and inertial properties. One-way flexural edge waves on straight chiral interfaces have been identified here. To the best of our knowledge, this has never been achieved in the past.

Acknowledgements

All authors would like to thank the EPSRC (UK) for its support through Programme Grant no. EP/L024926/1.

References

[1] Thomson W. 1894. *The Molecular Tactics of a Crystal*. 1st edn., Clarendon Press, Oxford.

[2] Prall D, Lakes RS. 1997. Properties of a chiral honeycomb with a Poisson's ratio of -1. *Int. J. Mech. Sci.* **39**, 305–314.

[3] Spadoni A, Ruzzene M. 2012. Elasto-static micropolar behavior of a chiral auxetic lattice. *J. Mech. Phys. Solids* **60**, 156–171.

[4] Wu W, Qi D, Liao H, Qian G, Geng L, Niu Y, Lian J. 2018. Deformation mechanism of innovative 3D chiral metamaterials. *Sci. Rep.* **8**, 12575.

[5] Bahaloo H, Li Y. 2019. Micropolar modeling of auxetic chiral lattices with tunable internal rotation. *J. Appl. Mech.* **86**, 041002.

[6] Spadoni A, Ruzzene M, Gonella S, Scarpa F. 2009. Phononic properties of hexagonal chiral lattices. *Wave Motion* **46**, 435–450.

[7] Tee KF, Spadoni A, Scarpa F, Ruzzene M. 2010. Wave propagation in auxetic tetrachiral honeycombs. *J. Vib. Acoust.* **132**, 031007.

[8] Wang Y-F, Wang Y-S, Zhang C. 2016. Two-dimensional locally resonant elastic metamaterials with chiral comb-like interlayers: Bandgap and simultaneously double negative properties. *J. Acoust. Soc. Am.* **139**, 3311.

[9] Zhu R, Liu XN, Hu GK, Sun CT, Huang GL. 2014. A chiral elastic metamaterial beam for broadband vibration suppression. *J. Sound Vib.* **333**, 2759–2773.

[10] Carta G, Jones IS, Movchan NV, Movchan AB, Nieves MJ. 2017. Gyroelastic beams for the vibration reduction of long flexural systems. *Proc. Math. Phys. Eng. Sci.* **473**, 20170136.

[11] Bigoni D, Guenneau S, Movchan AB, Brun M. 2013. Elastic metamaterials with inertial locally resonant structures: application to lensing and localization. *Phys. Rev. B* **87**, 174343.

[12] Tallarico D, Movchan NV, Movchan AB, Colquitt DJ. 2017. Tilted resonators in a triangular elastic lattice: Chirality, Bloch waves and negative refraction. *J. Mech. Phys. Solids* **103**, 236–256.

[13] Tallarico D, Trevisan A, Movchan NV, Movchan AB. 2017. Edge waves and localization in lattices containing tilted resonators. *Front. Mater.* **4**, 16.

[14] Bacigalupo A, Gambarotta L. 2014. Homogenization of periodic hexa- and tetrachiral cellular solids. *Compos. Struct.* **116**, 461–476.

[15] Carta G, Nieves MJ, Jones IS, Movchan NV, Movchan AB. 2018. Elastic chiral waveguides with gyro-hinges. *Quart. J. Mech. Appl. Math.* **71**, 157–185.

[16] Nieves MJ, Carta G, Jones IS, Movchan AB, Movchan NV. 2018. Vibrations and elastic waves in chiral multi-structures. *J. Mech. Phys. Solids* **121**, 387–408.

[17] D'Eleuterio GMT, Hughes PC. 1984. Dynamics of gyroelastic continua. *J. Appl. Mech.* **51**, 415–422.

[18] Hughes PC, D'Eleuterio GMT. 1986. Modal parameter analysis of gyroelastic continua. *J. Appl. Mech.* **53**, 918–924.

[19] D'Eleuterio GMT. 1988. On the theory of gyroelasticity. *J. Appl. Mech.* **55**, 488–489.

[20] Yamanaka K, Heppler GR, Huseyin K. 1996. Stability of gyroelastic beams. *AIAA J.* **34**, 1270–1278.

[21] Hassanpour S, Heppler GR. 2016. Dynamics of 3D Timoshenko gyroelastic beams with large attitude changes for the gyros. *Acta Astron.* **118**, 33–48.

[22] Brun M, Jones IS, Movchan AB. 2012. Vortex-type elastic structured media and dynamic shielding. *Proc. R. Soc. A* **468**, 3027–3046.

[23] Carta G, Brun M, Movchan AB, Movchan NV, Jones IS. 2014. Dispersion properties of vortex-type monatomic lattices. *Int. J. Solids Struct.* **51**, 2213–2225.

[24] Carta G, Jones IS, Movchan NV, Movchan AB, Nieves MJ. 2017. "Deflecting elastic prism" and unidirectional localisation for waves in chiral elastic systems. *Sci. Rep.* **7**, 26.

[25] Colquitt DJ, Movchan NV, Movchan AB. 2016. Parabolic metamaterials and Dirac bridges. *J. Mech. Phys. Solids* **95**, 621–631.

[26] Raghu S, Haldane FDM. 2008. Analogs of quantum-Hall-effect edge states in photonic crystals. *Phys. Rev. A* **78**, 033834.

[27] Wang Z, Chong YD, Joannopoulos JD, Soljačić M. 2008. Reflection-free one-way edge modes in a gyromagnetic photonic crystal. *Phys. Rev. Lett.* **100**, 013905.

[28] He C, Chen XL, Lu MH, Li XF, Wan WW, Qian XS, Yin RC, Chen YF. 2010. Left-handed and right-handed one-way edge modes in a gyromagnetic photonic crystal. *J. Appl. Phys.* **107**, 123117.

[29] Khanikaev AB, Mousavi SH, Tse WK, Kargarian M, MacDonald AH, Shvets G. 2013. Photonic topological insulators. *Nature Mater.* **12**, 233–239.

[30] Gao W, Lawrence M, Yang B, Liu F, Fang F, Béri J, Li J, Zhang S. 2015. Topological photonic phase in chiral hyperbolic metamaterials. *Phys. Rev. Lett.* **114**, 037402.

[31] Pal RK, Ruzzene M. 2017. Edge waves in plates with resonators: an elastic analogue of the quantum valley Hall effect. *New J. Phys.* **19**, 025001.

[32] Jin Y, Torrent D, Djafari-Rouhani B. 2018. Robustness of conventional and topologically protected edge states in phononic crystal plates. *Phys. Rev. B* **98**, 054307.

[33] Makwana MP, Craster RV. 2018. Geometrically navigating topological platonic modes around gentle and sharp bends. *Phys. Rev. B* **98**, 184105.

[34] Makwana MP, Craster RV. 2018. Designing multi-directional energy-splitters and topological valley supernetworks. *Phys. Rev. B* **98**, 235125.

[35] Chaplain GJ, Makwana MP, Craster RV. 2019. Rayleigh-Bloch, topological edge and interface waves for structured elastic plates. *Wave Motion* **86**, 162–174.

[36] Zheng L-Y, Teocharis G, Tournat V, Gusev V. 2018. Quasitopological rotational waves in mechanical granular graphene. *Phys. Rev. B* **97**, 060101(R).

[37] Süsstrunk R, Huber SD. 2015. Observation of phononic helical edge states in a mechanical topological insulator. *Science* **349**, 6243, 47–50.

[38] Wang P, Lu L, Bertoldi K. 2015. Topological phononic crystals with one-way elastic edge waves. *Phys. Rev. Lett.* **115**, 104302.

[39] Nash LM, Kleckner D, Read A, Vitelli V, Turner AM, Irvine WTM. 2015. Topological mechanics of gyroscopic metamaterials. *Proc. Natl. Acad. Sci.* **112**, 14495–14500.

[40] Garau M, Carta G, Nieves MJ, Jones IS, Movchan NV, Movchan AB. 2018. Interfacial waveforms in chiral lattices with gyroscopic spinners. *Proc. Roy. Soc. A.* **474**, 20180132.

[41] Evans DV, Porter R. 2007. Penetration of flexural waves through a periodically constrained thin elastic plate floating on water. *J. Eng. Math.* **58**, 317–337.

[42] Haslinger SG, Movchan NV, Movchan AB, McPhedran RC. 2012. Transmission, trapping and filtering of waves in periodically constrained elastic plates. *Proc. Roy. Soc. A.* **468**, 76–93.

[43] Haslinger SG, Movchan AB, Movchan NV, McPhedran RC. 2014. Symmetry and resonant modes in platonic grating stacks. *Waves Random Complex Media* **24**, 126–148.

[44] Haslinger SG, Craster RV, Movchan AB, Movchan NV, Jones IS. 2016. Dynamic interfacial trapping of flexural waves in structured plates. *Proc. Roy. Soc. A.* **472**, 20150658.

[45] Haslinger SG, Movchan NV, Movchan AB, Jones IS, Craster RV. 2017. Controlling flexural waves in semi-infinite platonic crystals with resonator-type scatterers. *Q. J. Mech. Appl. Math.* **70**, 216–247.

[46] Haslinger SG, Jones IS, Movchan NV, Movchan AB. 2018. Localisation in semi-infinite herringbone waveguides. *Proc. R. Soc. A* **474**, 20170590.

[47] Movchan AB, McPhedran RC, Carta G, Craster RV. 2019. Platonic localisation: one ring to bind them. *Arch. Appl. Mech.* **89**, 521–533.

[48] Cai L-W, Hambric SA. 2016. Movable rigid scatterer model for flexural wave scattering on thin plates. *J. Vib. Acoust.* **138**, 031016.

[49] COMSOL Multiphysics®v. 5.4. www.comsol.com. COMSOL AB, Stockholm, Sweden.

[50] Genta G. 2005. *Dynamics of Rotating Systems*. Springer Science+Business Media, Inc., Mechanical Engineering Series.

[51] Song O, Kwon HD, Librescu L. 2001. Modeling, vibration, and stability of elastically tailored composite thin-walled beams carrying a spinning tip rotor. *J. Acoust. Soc. Am.* **110**(2), 877–886 .

[52] Melnikov YA. 2001. Green's function of a thin circular plate with elastically supported edge. *Eng. Anal. Bound. Elem.* **25**, 669–676.

[53] Carta G, Nieves MJ, Jones IS, Movchan NV, Movchan AB. 2019. Flexural vibration systems with gyroscopic spinners. To appear in *Phil. Trans. Royal Soc. London A*.

Appendix. Regularisation procedure for the determination of the dispersion diagrams

In this section, we describe the semi-analytical approach that has been used to determine the dispersion diagrams of the infinite plate connected to a doubly-periodic array of chiral resonators. In particular, we derive analytically the system of equations and then we find numerically the roots of the determinant of the system, which yield the dispersion diagrams of the periodic structure.

We consider an elementary rectangular cell, with $\boldsymbol{x} \in (-d_x/2, d_x/2) \times (-d_y/2, d_y/2)$, connected to a chiral resonator at the origin. The transverse displacement and rotations at $\boldsymbol{x} = (0, 0)$ are indicated by

$$W_{\rm P}|_{x=y=0} = \delta_z, \qquad \nabla W_{\rm P}|_{x=y=0} = \begin{pmatrix} \alpha_x \\ \alpha_y \end{pmatrix}. \tag{A.1}$$

The displacement and rotations at the origin can be obtained by summing all the contributions due to the axial forces and bending moments transmitted by

the beams to the plate. These contributions can be evaluated by employing the Green's function.

The static Green's function in the infinite plate cannot be used for the evaluation of the lattice sums because it does not decay at infinity. Hence, for the purpose of the analysis of Bloch-Floquet waves, we use the following regularisation procedure.

First, we truncate the lattice sums to order N (in the illustrative calculations of Section 3.2, $N = 200$). Then, we use the Green's function (20) for a circular massless plate of radius $R = 2N\max(d_x, d_y)$, which contains all the $N \times N$ chiral resonators. We denote by $G(x, y, \xi, \eta)$, $\mu_x(x, y, \xi, \eta)$ and $\mu_y(x, y, \xi, \eta)$ the displacements evaluated at the point (x, y) produced by a unit force, a unit moment around the x-axis and a unit moment around the y-axis, respectively, applied at the point (ξ, η). Accordingly, the displacement and rotations at the origin of the elementary cell can be determined as follows:

$$\begin{aligned}
W_{\rm p}|_{x=0,y=0} &= \sum_{n=-N}^{N}\sum_{m=-N}^{N} \mathrm{e}^{\mathrm{i}\gamma_{mn}} \left\{\mathscr{N}\delta_z G(0,0,nd_x,md_y) + [\mathscr{M}_1\alpha_x + \mathscr{M}_2\alpha_y]\right. \\
&\quad \left.\times\mu_x(0,0,nd_x,md_y) + [-\mathscr{M}_2\alpha_x + \mathscr{M}_1\alpha_y]\,\mu_y(0,0,nd_x,md_y)\right\}\,, \\
\left.\frac{\partial W_{\rm p}}{\partial y}\right|_{x=0,y=0} &= \sum_{n=-N}^{N}\sum_{m=-N}^{N} \mathrm{e}^{\mathrm{i}\gamma_{mn}} \left\{\mathscr{N}\delta_z \frac{\partial G}{\partial y}(0,0,nd_x,md_y) + [\mathscr{M}_1\alpha_x + \mathscr{M}_2\alpha_y]\right. \\
&\quad \left.\times\frac{\partial \mu_x}{\partial y}(0,0,nd_x,md_y) + [-\mathscr{M}_2\alpha_x + \mathscr{M}_1\alpha_y]\,\frac{\partial \mu_y}{\partial y}(0,0,nd_x,md_y)\right\}\,, \\
\left.\frac{\partial W_{\rm p}}{\partial x}\right|_{x=0,y=0} &= \sum_{n=-N}^{N}\sum_{m=-N}^{N} \mathrm{e}^{\mathrm{i}\gamma_{mn}} \left\{\mathscr{N}\delta_z \frac{\partial G}{\partial x}(0,0,nd_x,md_y) + [\mathscr{M}_1\alpha_x + \mathscr{M}_2\alpha_y]\right. \\
&\quad \left.\times\frac{\partial \mu_x}{\partial x}(0,0,nd_x,md_y) + [-\mathscr{M}_2\alpha_x + \mathscr{M}_1\alpha_y]\,\frac{\partial \mu_y}{\partial x}(0,0,nd_x,md_y)\right\}\,.
\end{aligned} \tag{A.2}$$

Here $\gamma_{mn} = k_x nd_x + k_y md_y$, where $\boldsymbol{k} = (k_x, k_y)^{\rm T}$ is the wave vector. In addition, as in Section 3.2, $N_z(0) = \mathscr{N}\delta_z$, $M_x(0) = \mathscr{M}_1\alpha_x + \mathscr{M}_2\alpha_y$ and $M_y(0) = -\mathscr{M}_2\alpha_x + \mathscr{M}_1\alpha_y$ are the axial force and bending moments transmitted to the plate by the beam attached at the origin of the elementary cell. The quantities $\mathscr{N}$, $\mathscr{M}_1$ and $\mathscr{M}_2$ are given in (33). In order to account for the contributions of all the beams, Bloch-Floquet conditions for the axial forces and bending moments have been used in (A.2).

Combining (A.1) and (A.2), we obtain a homogeneous system of three equations in the three unknowns δ_z, α_x and α_y. Non-trivial solutions of this system are obtained by setting the determinant of the matrix containing the coefficients of δ_z, α_x and α_y equal to zero. This leads to the *dispersion relation* of the system, which shows how the radian frequency ω (appearing in $\mathscr{N}$, $\mathscr{M}_1$ and $\mathscr{M}_2$) depends on the wave vector $\boldsymbol{k}$. The dispersion relation is solved numerically and the dispersion diagrams represented by the solid grey lines in Fig. 5 are obtained.